High Voltage

WILEY

国家电网 STATE GRID 中国电力科学研究院有限公司 CHINA ELECTRIC POWER RESEARCH INSTITUTE | IET The Institution of Engineering and Technology

ORIGINAL RESEARCH OPEN ACCESS

Breakdown and Discharge Characteristics of High Repetition Frequency Nanosecond Pulsed Air Dielectric Barrier Discharge

Mahreen[1] | Dongxuan Xu[1] | Denis Shaw[2] | Peter Bruggeman[1]

[1]Department of Mechanical Engineering, University of Minnesota, Minneapolis, Minnesota, USA | [2]Advanced Energy Industries Inc., Fort Collins, Colorado, USA

Correspondence: Peter Bruggeman (pbruggem@umn.edu)

Received: 21 January 2025 | **Revised:** 25 April 2025 | **Accepted:** 22 May 2025

Associate Editor: Cheng Zhang

ABSTRACT

This study explores the breakdown characteristics and discharge modes in a parallel plate air dielectric barrier discharge system using repetitive nanosecond pulses, with pulse repetition frequencies (PRFs) from 0.1 to 100 kHz. It examines how pulse parameters—PRF, pulse number and gas pressure—affect the memory effect, leveraging current and voltage measurements, fast imaging and optical emission spectroscopy. The findings show that higher PRFs lead to a reduction in breakdown voltage well below the streamer breakdown threshold. We argue that this effect may be attributed to the cumulative buildup of metastable species and negative ions in the discharge gap which could sustain free electrons in-between the voltage pulses. Despite observing increased energy deposition with higher PRFs, the impact on filament formation was minimal, highlighting a strong dependence of discharge morphology on the accumulation of plasma-produced species. This research studies provides valuable insights for controlling discharge regimes in applications such as plasma-assisted combustion, surface treatment and air treatment by clarifying the interactions between discharge mechanisms at different PRFs and pressures.

1 | Introduction

With recent progress in pulsed power systems, commercial high-voltage devices are now capable of delivering nanosecond voltage pulses at repetition frequencies ≤ 100 kHz [1–3], although a few studies have explored higher repetition rates in burst studies [4]. These ultra-fast, repetitive pulses allow for effective energy deposition into plasmas, while sustaining a highly reduced electric field (E/n) and driving electron temperatures (T_e) to levels more than 100 times higher than the ambient gas temperature [5, 6]. Nonequilibrium plasmas operated with nanosecond pulses support a range of high-energy electron-driven chemical processes, such as plasma-assisted combustion, surface decontamination, ozone generation, and air treatment such as NO_x removal [7–14].

At atmospheric pressure, streamer breakdown is the most common breakdown mechanism [15–18]. Electron avalanches create a space charge, and this self-generated electric field enhances the growth of secondary electron avalanches near space charge regions. Consequently, the ionised region and the perturbation of the electric field grow rapidly and form distinct plasma channels, called streamers. The Raether–Meek criterion states that the threshold for streamer formation can be estimated by the product of the effective ionisation coefficient α_{eff} and the distance d equal to 18 [15]. However, in a few cases, a deviation from the streamer breakdown was observed in atmospheric air dielectric barrier discharges (DBDs). Starostin et al. reported $\alpha_{eff}d \approx 10$, considerably lower than the Raether–Meek criterion for streamer formation [19]. Montijn el al. reinvestigated the Raether–Meek criterion and showed that the streamer emergence depends not

only on the ionisation rate, the attachment rate and the gap length, but also on electron diffusion [20]. Based on physical and analytical considerations, it was suggested that the quantitative predictions require a diffusive correction to this criterion for accurate predictions. The initial electrons that start the discharge formation can be provided by radioactivity, photoionisation and the leftover charges in the gap from previous discharges, which we refer to as the 'volume memory effect' [5, 18].

Plasma physics phenomena, such as breakdown mechanisms, fast gas heating, discharge regime transitions and volume memory effects, have gained increasing attention, as these mechanisms are fundamental to the evolution of repetitively pulsed discharges [5, 21–24]. Ultimately the memory effect is crucial for understanding the discharge mode and achieving predictive control on plasma properties. Discharge mode transitions remain universal challenges that complicate efforts to achieve reliable and stable operation. In plasma-assisted combustion, high repetition frequency nanosecond pulsed discharges in pin–pin geometries are frequently used, which allows glow-mode operation at moderate voltages in air [25]. However, spark discharges can still occur even with 10 ns pulse durations, driven by the cumulative effects across multiple discharge pulses or fast gas heating and stepwise ionisation. Discharge electrode geometry, electrode properties, gas composition and flow dynamics all significantly influence the discharge behaviour and its instabilities [26–28]. Utilising DBDs helps to prevent streamer-to-spark transitions, as the dielectric barrier limits the charge transferred through the plasma channel [29]. The constructive collaboration between DBDs and nanosecond voltage pulses facilitates uniform discharge regimes at atmospheric pressure [22, 30, 31]. The manipulation of the discharge mode is also crucial for enabling controllable chemical reactions and processing conditions. The discharge mode transition refers to (i) modulations by pulse parameters and (ii) progressive transitions in the same long pulse train (e.g., formation of the gas gap breakdown). Several computational and experimental studies of pulsed nanosecond DBDs have been pursued which reveal different discharge regimes, including filamentary microdischarges and diffuse glow and Towsend discharges [23, 30, 31]. Prior studies have explored the influence of electrical parameters on the discharge homogeneity (mainly pulse voltage amplitudes and frequencies, pulse rise times, the influence of the airflow and the local electric field) [22, 23, 32, 33]. However, there is no comprehensive qualitative understanding of how to control the different discharge homogeneity.

Intrinsic to repetitively pulsed and dielectric barrier discharges, the volume memory effect plays a pivotal role in elucidating the evolution of discharge dynamics and breakdown phenomena [34–36]. In a systematic investigation, Shao et al. characterised gas gap breakdown under repetitive nanosecond pulses (30 ns duration, pulse repetition frequency (PRF): 0–1 kHz), introducing key parameters such as the breakdown electric field strength, the breakdown time lag (the time interval between the initial displacement current and the subsequent discharge current rise), the repetitive stressing time (time duration between two consecutive voltage pulses) and the number of applied pulses before breakdown occurs [36]. Their findings revealed nonlinear dependencies between the breakdown field strength and stressing time as a function of the PRF, which were attributed to the cumulative presence of metastable and excited species. Similarly, Zhao et al. explored the evolution of corona discharge dynamics in high-pressure nitrogen under repetitive sub-microsecond pulses (800 ns duration, PRF: 0.02 Hz–2 kHz), identifying a space–charge-dominated volume memory effect and the influence of the space–charge region on the electric field spatial distribution [37]. In a recent experimental study, DBD plasma assisted ignition for methane-air flow was investigated [38]. The work aimed to characterise the effects of pulse repetition on pulse-to-pulse coupling and its ability to ignite methane-air flows and showed the important effect of combustion chemistry on plasma stability [38, 39].

At sufficiently high PRF, a decreasing trend in breakdown voltage under repetitively pulsed discharges has been observed, but specific agents responsible for this memory effect and their simultaneous impact on subsequent discharges at higher PRFs remain unclear [40]. Metastable species, free electrons, negative ions, gas heating and surface charges on dielectrics are the memory agents reported in previous theoretical and experimental investigations [30, 36, 40]. A double-pulse method has been used to simulate repetitive pulses probably because of the technical difficulty in designing a repetitive pulse generator at a high voltage and high PRF with a stable voltage waveform [37]. Nijdam et al. discovered that for a short duration of two discharge pulses (in low-pressure N_2–O_2 mixture), the development of the second streamer experienced several distinct stages with increasing the pulse interval time [41]. For the extremely short pulse time interval (~100 ns), the second streamer would continue where the first one stopped at the end of the first voltage pulse. On the other hand, if the pulse interval time was slightly longer (~tens of μs), the second streamer occupied new channels and preferably developed at the edges of previous streamer channels. Li et al. observed breakdown recovery in pin-to-pin nanosecond pulsed spark discharges on timescales of 50–100 μs which was attributed to plasma-induced gas rarefaction [42].

It is noteworthy that experimental investigations of breakdown mechanisms at high repetition frequencies (> 10 kHz) and qualitative analysis of memory effects are not explored yet in DBDs which could consist of both volume and surface memory effects on the dielectric barriers. We used a parallel plate air DBD generated by repetitively pulsed nanosecond pulses with a repetition frequency varying over three orders of magnitude, that is, 0.1–100 kHz. Our aim is to focus on the impact of the memory effect on breakdown characteristics, energy coupling and discharge morphology.

2 | Experimental Set-Up and Methods

This section outlines the experimental setup, describes the nanosecond plasma dielectric barrier discharge system and details the measurement techniques used.

2.1 | Plasma Source

A schematic diagram of the experimental setup is shown in Figure 1a. The plasma reactor was operated in ambient air by a

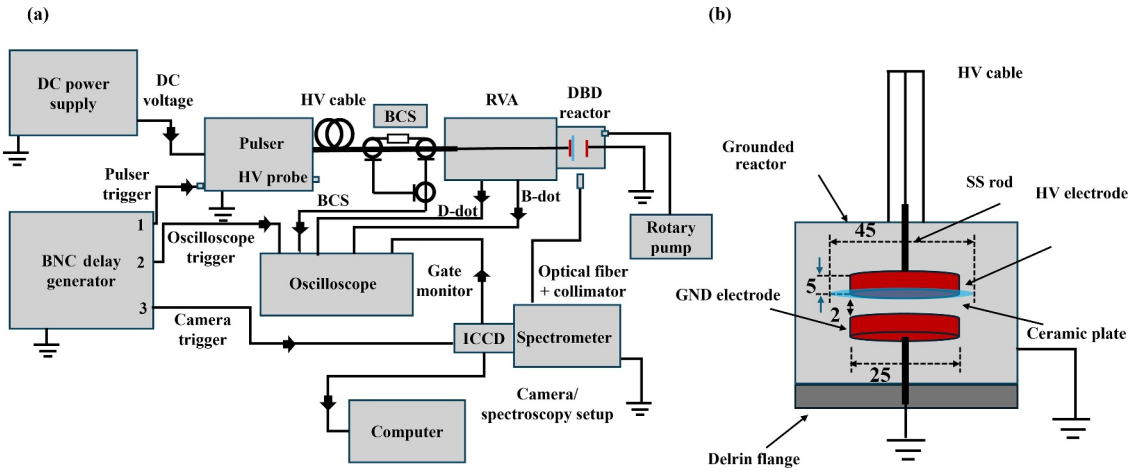

FIGURE 1 | Schematic of the experimental setup and the implemented diagnostics. (a) Overview; (b) cross-sectional view of the DBD reactor with electrode dimensions in mm. The figure is not to scale.

high-voltage pulser (Transient Plasma System SSPG-20X-100K-1 kW), which generates positive polarity voltage pulses with a maximum amplitude of ~15 kV. The pulses have a rise time (10%–90%) of 8–12 ns, a pulse duration (full width at half maximum, FWHM) of 15–25 ns, and a maximum pulse repetition frequency of 100 kHz. The pulse amplitude was controlled by adjusting the output voltage of a DC power supply (Magna Power SL 1500-1.7/208), and the pulse repetition frequency was varied using an arbitrary function generator (Tektronix AFG-2021). High-voltage pulses were delivered to a homemade coaxial rod vessel assembly (RVA) using a 50 Ω, high voltage (HV) coaxial line. The 10-m length of the coaxial line allowed us to separate the forward pulse from the reflected pulse that oscillates between the pulser and the plasma reactor. Pulses were detected by a custom-made back current shunt (BCS) mounted on the coaxial line. The RVA delivered the high-voltage pulses to the HV electrode for plasma generation in the plasma reactor and was equipped with homemade voltage (D-dot) and current (B-dot) sensors [43, 44].

The nanosecond high-voltage pulse trigger is time-synchronised with an intensified charge-coupled device (ICCD) camera (Andor iStar DH340T) for imaging. The optical emission spectrometer (Jobin Yvon spectrometer HR 640) backed with the same ICCD was used to determine the gas temperature. A 4-channel delay generator (BNC 577) was used to synchronise the detector with plasma generation. All electrical waveforms were recorded by a 350 MHz bandwidth digital oscilloscope (Rigol MSO5354). The pulse generator was operated in both continuous and burst mode.

The plasma reactor was a custom-built parallel plate DBD system. A cross-sectional view of the reactor is depicted in Figure 1b. It features two parallel circular electrodes made of stainless steel, each with a diameter of 25 mm and a thickness of 5 mm, housed within a 3.38-inch 6-way conflat cube. The electrodes have rounded edges to avoid the increase in the electric field near the edges. An alumina plate (45 mm in diameter and 1 mm thick) is mounted on the HV electrode, functioning as a dielectric barrier. The discharge gap was kept fixed at 2 mm. Two quartz observation windows were positioned on the sides of the housing to allow for optical diagnostics. The air pressure inside the reactor was regulated by a rotary pump (Edwards nXDS6i) and adjusted between 10 and 760 Torr for different experimental conditions. The operating pressure was monitored using a digital vacuum transducer (MKS PDR900-1).

2.2 | Energy Measurements

A custom energy measurement system was developed by integrating a tailored BCS and designing a RVA system. This system incorporated homemade D-dot and B-dot sensors mounted on the RVA to measure the load voltage and current. The RVA was filled with transformer oil with a dielectric permittivity, $\varepsilon_r = 2.2$ and its impedance was engineered to match the 50 Ω impedance of the high-voltage cable. A solid aluminium rod (O.D. = 12 mm) was positioned at the centre of a hollow cylindrical stainless-steel vessel (I.D. = 42.6 mm), forming a coaxial assembly. This configuration enabled precise voltage and current measurements at the plasma load. D-dot and B-dot sensors operated in the 'integration regime', where the high voltage and current were proportional to the integral of the sensors' waveform [43, 44]. The high voltage and the high voltage line current can be reconstructed from the D-dot and B-dot readout V_{Ddot} and V_{Bdot} as follows:

$$V_{\mathrm{HV}}(t) = A_{\mathrm{Ddot}} \int V_{\mathrm{Ddot}}\, \mathrm{d}t, \tag{1a}$$

$$I_{\mathrm{HV}}(t) = A_{\mathrm{Bdot}} \int V_{\mathrm{Bdot}}\, \mathrm{d}t. \tag{1b}$$

A_{Ddot} and A_{Bdot} are the calibration coefficients equal to 2.1×10^{12} V/V and 6.9×10^{9} A/V, respectively, and t represents time. D-dot and B-dot sensors were calibrated using a standard 75 MHz HV probe (Tektronix P6015A) and a 200 MHz current transformer (Pearson Electronics 2877), respectively, and the synchronisation between these sensors was achieved by aligning the voltage time derivative with the current waveform for a capacitive load (without discharge). The pulse energy coupled to the plasma was calculated using the following equation:

$$E_p = \int V_{HV}(t) \, . \, I_{HV}(t) \, dt. \quad (2)$$

The BCS sensor was employed to accurately differentiate the reflected pulse travelling back towards the pulser from the forward pulse. The pulse energy was validated using the BCS technique to calculate the energy associated with a single pulse. This specialised shunt was designed for measuring fast signals propagating through a 10 m coaxial cable. It is constructed by replacing a section of the outer conducting braid of the coaxial cable with an array of five identical non-inductive 1 Ω resistors connected in parallel, resulting in an overall shunt resistance (R_{Sh}) of 0.2 Ω. To calibrate the shunt resistor, a known signal of desired pulse parameters was applied from a function generator, and the voltage across the shunt (V_{Sh}) was directly measured using a digital oscilloscope configured to match the impedance of the high-voltage coaxial cable (50 Ω). During plasma measurements, a 20 dB signal attenuator is employed to safeguard the oscilloscope from a potential voltage overload. Further details on the design and implementation of the BCS can be found in refs. [45, 46]. With a known HV cable impedance ($Z_0 = 50$ Ω) and assuming that the ground wire and the centre wire currents are equal, the voltage in the centre wire can be written as follows:

$$V_{HV} = \frac{V_{Sh} Z_0}{R_{Sh}}. \quad (3)$$

The pulse energy can be calculated as follows:

$$E_p = \int_{pulse} \frac{{V_{HV}}^2}{Z_0} dt. \quad (4)$$

The actual energy deposited in the discharge can be computed by subtracting the energy of the reflected pulse $E_{p,REF}$ from that of the forward pulse $E_{p,FWD}$.

2.3 | Optical Measurements

High speed imaging and optical emission spectroscopy over a range of PRF and pulse numbers (N) captured the pulse-to-pulse plasma morphology within a single burst and measured the pulse-to-pulse change in the gas temperature using the second positive system of nitrogen, N_2 (C→B) (0–0).

For single-shot imaging, a total of 100 pulses were applied in a single burst, and images were recorded for pulse numbers $N = 1$, 10, 50, and 100. For image visualisation, the camera exposure time was set equal to the pulse interval for each frequency, for example, for capturing a 100 kHz PRF signal the exposure time was set to 10 μs. The exposure time was sufficient to capture most of the plasma emission over the range of operating conditions tested. The gate width was fixed at 50 ns to enable capturing of one voltage pulse. The gain was 2000 for all measurements.

N_2 (C→B) (0–0) emission spectra (at 337 nm) were captured with an optical fibre cable along with a collimating lens and recorded by an ICCD at the spectrometer exit. The spectrometer had an 1800 g/mm diffraction grating with an instrumental line profile FWHM of 0.071 nm. The slit function was recorded by a low-pressure mercury–argon pen lamp. The pulse generator operated at a burst frequency of 1 Hz during optical emission spectroscopy (OES) measurements, allowing data to accumulate from 50 to 500 times due to varying plasma emission intensity over the low pressure to atmospheric pressure conditions investigated. Each burst consisted of 100 HV pulses, and measurements were taken for pulse numbers $N = 1$, 10, 50, and 100. The ICCD camera was synchronised and triggered during the HV pulse with a gate width of 50 ns. This allowed for the measurement of the pulse-average gas temperature. The exposure time of the camera was kept fixed at 1 μs. The value of the gas temperature, which is in good approximation equal to the rotational temperature of the N_2 (C→B) spectra [47], is estimated by fitting the theoretically predicted synthetic spectrum to the experimentally recorded spectrum of N_2 (C→B) (0,0) at 337 nm using Specair [48]. A sample emission spectrum of the ro-vibrational spectrum for the 1st and 100th pulse is shown in Figure 2, where gas temperature = (380 ± 50) K and (1000 ± 50) K are for $N = 1$ and 100, respectively. ICCD settings are 50 ns gate width, 1 s exposure time and 50 accumulations. The image shows the best fit of the simulation spectra to the experimental spectra.

3 | Results and Discussion

The primary objective of this study is to investigate the influence of the pulse repetition frequency on the electrical and morphological properties of the DBD plasma. First, we report the analysis of the breakdown characteristics of high-frequency nanosecond pulse discharge in air. Subsequently, we present findings on the electrical behaviour, the visualisation of discharge patterns and gas heating.

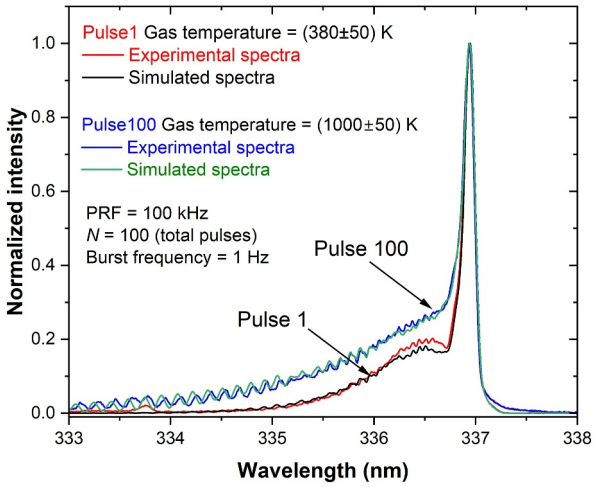

FIGURE 2 | N_2 (C→B) (0–0) emission spectrum for pulse numbers, $N = 1$ and 100 in a 100 kHz pulse discharge generated in atmospheric pressure air at 8 kV voltage.

3.1 | Breakdown Mechanism in High-Frequency Nanosecond Pulsed Discharges

3.1.1 | Impact of Pulse Repetition Frequency

We investigate the applied voltage enabling breakdown as shown in Figure 3 at atmospheric pressure by increasing the PRF from 0.1 to 100 kHz in the continuous excitation mode. The different threshold voltages relevant for ionisation and breakdown processes are provided. α and η are ionisation and attachment coefficients, respectively. The 'breakdown voltage' was determined by the applied voltage at which optical emission was observed. The air gap voltage is without the presence of surface charge approximately 5% lower than the applied voltage (capacitive voltage divider). To account for the memory effect in the breakdown phenomenon, a one-minute waiting period was implemented between two subsequent voltage increases in steps of 250 V. Hence, we do not refer here to the steady-state breakdown voltage typically used in AC-driven DBD studies. The D-dot probe was used to measure the applied voltage. We found a significant reduction in the applied voltage leading to breakdown with increasing PRF, from approximately 13 kV for 0.1 kHz to 6 kV for 100 kHz PRF. This result highlights the substantial influence of memory effects on the breakdown characteristics at high PRFs.

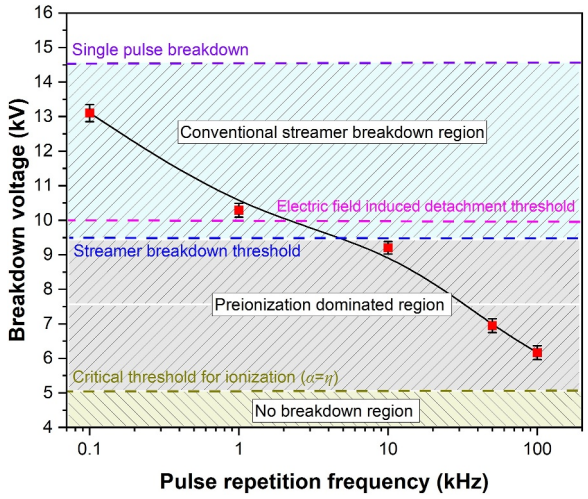

FIGURE 3 | Applied voltage required to achieve breakdown (referred to as breakdown voltage) for various PRF in atmospheric pressure air at continuous pulse operation.

Essentially, the Raether–Meek criterion describes the conditions for streamer formation. It postulates that an electron avalanche propagating in a gas with an electron drift velocity transforms into a streamer when the total number of electrons in the avalanche tip reaches ~10^8, which corresponds to $\alpha_{\text{eff}} d = (\alpha - \eta)\, d \geq 18$ [4, 15]. The ionisation and attachment coefficient are dependent on the reduced electric field. For electrode gaps with a nonuniform electric field, the generalised Raether–Meek criterion is formulated by $\int_0^d \alpha_{\text{eff}}\, \mathrm{d}x \approx 18$ with d as the inter-electrode gap [15]. In the case of nanosecond voltage pulses one can estimate the threshold voltage for streamer breakdown by formulating the criterion for a finite pulse duration as follows [49]:

$$\int_0^t \nu_{\text{iz}}\, \mathrm{d}t = 18, \tag{5}$$

with ν_{iz} be the ionisation frequency. The drift velocity is the product of the electron mobility (μ_e) and the electric field (E). The integral is performed over the duration of voltage pulse and considered only for the positive values of α_{eff}.

$$\int_0^t \alpha_{\text{eff}}\, \nu_{\text{d}}\, \mathrm{d}t = \int_0^t \alpha_{\text{eff}} \mu_e E\, \mathrm{d}t = \int_0^t \left(\frac{\alpha_{\text{eff}}}{n}\right)(\mu_e n)(E)\mathrm{d}t = 18, \tag{6}$$

with ν_{d} is the electron drift velocity and n is the air density. The values of α_{eff}/n and $\mu_e n$ in air were taken from ref. [49]. The critical electric field is defined as the reduced electric field at which the effective ionisation coefficient tends to zero ($\alpha_{\text{eff}} = 0$) which equals 94 Td [49]. This threshold represents a necessary lower bound for the background electric field as an electron avalanche cannot develop for lower reduced electric fields. The voltage corresponding to the streamer breakdown threshold was calculated from Equation (6) and yields ~9.5 kV. At lower PRFs (< 10 kHz), the applied voltage is larger than the streamer breakdown voltage; however, at higher PRFs the applied voltage is well below the threshold for streamer breakdown and starts even to approach the critical electric field at a PRF of 100 kHz.

Electron attachment is the predominant mechanism for electron loss in air plasma [50]. The lifetime of free electrons in this environment is estimated to be around 20 ns, corresponding to the timescale of three-body electron attachment reactions involving O_2 [51]. A list of reactions critical for the generation and loss of electrons in the afterglow is provided in Table 1. Due

TABLE 1 | Most dominant electron production and destruction reactions along with the rate constants.

Reaction		Rate constant (cm^3/s or cm^6/s)	Reference
R_1	$e^- + O_2 + M \rightarrow O_2^- + M$	$k_1 = 1 \times 10^{-31}$	[52]
R_2	$O_2{}^- + M \rightarrow O_2 + M + e^-$	$k_2 = 2.7 \times 10^{-10} \sqrt{T/300}\, \exp(-5590/T)$	[49]
R_3	$O^- + M \rightarrow O + M + e^-$	$k_3 = 1.9 \times 10^{-12} \sqrt{T/300}\, \exp(-4990/T)$	[49]
R_4	$O_2(a^1\Delta_g) + O_2 \rightarrow 2O_2$	$k_4 = 3.0 \times 10^{-18} \exp(-200/T)$	[53]
R_5	$O_2{}^- + O_2(a^1\Delta_g) \rightarrow 2O_2 + e^-$	$k_5 = 2 \times 10^{-10}$	[52]

to the rapid quenching of electrons in the discharge region, breakdown is largely dependent on the process of electron detachment. For air plasma, processes such as detachment from O^- and O_2^- can provide electrons to start a streamer discharge under the action of an electric field by ion-neutral collision [50, 51]. At atmospheric pressure, the generation of O_2^- ions is the most dominant mechanism [52]. One can compute the detachment time which is highly sensitive to the electric field strength and varies from 500 ns at 3 MV/m to only 10 ns at 5 MV/m [52, 53]. In our case, by considering the nanosecond pulse width (τ_p) equal to the electron detachment time (τ_d), the corresponding threshold voltage for electric field-induced detachment was estimated to be approximately 10 kV (this threshold is marked in Figure 3). This mechanism can produce electrons facilitating conventional streamer breakdown even in the case when no free electrons (and only negative ions) remain in the discharge gap. The observed breakdown voltages for PRF < 10 kHz allow for electric field-induced detachment.

Interestingly for PRFs exceeding 10 kHz, contrary to the streamer theory predictions, breakdown occurred at applied voltages considerably lower than those typically required for streamer inception. We hypothesise this is due to the buildup of charged and metastable species, such as $O_2(a^1\Delta_g)$ in air discharges [54], over multiple voltage pulses before breakdown occurs. The electronically excited metastable $O_2(a^1\Delta_g)$, also referred to as singlet oxygen, has been shown to be effective in electron detachment from negative ions (O^- and O_2^-) in the afterglow region of Ar + O_2 (1%) radio frequency (RF) plasma jet [55]. In the afterglow region, the $O_2(a^1\Delta_g)$ density was found to be as high as ~10^{16} cm^{-3} which contributed to the production of an electron density ~3 times higher than the O_2^- absolute density. The estimation confirmed the role of electrons and negative ions in the observed memory effect for high modulation frequencies (> 1 kHz), where electrons were found to be the most dominant negative charge carrier in the afterglow [55].

The lifetime of $O_2(a^1\Delta_g)$ is determined by collisional quenching in atmospheric pressure air [56, 57] and can be estimated as $\tau_{eff} = \frac{1}{k_4[O_2]}$ (see Table 1.) k_i is the rate constant for the ith reaction in units cm^3/s or cm^6/s for a binary or three body reaction with a species M, and T is the gas temperature in K. The obtained estimated lifetime of an $O_2(a^1\Delta_g)$ metastable is ~100 ms which is likely further reduced when O_3 is building up in the discharge gap. The dominant electron production pathway in air discharge is due to the collision of $O_2(a^1\Delta_g)$ with the O_2^- ion [58].

The decay of the negative ion (O_2^-) density in the afterglow can be estimated from the following relation describing positive–negative ion recombination process and assuming that the positive and negative ion densities ([n^+] and [n^-], respectively) are equal.

$$\frac{[n^-]}{[n_0^-]} = \frac{1}{1 + t\, k_r [n_0^-]} \tag{7}$$

Given the typical maximum negative ion density ~10^{14} cm^{-3} observed in air DBDs at atmospheric pressure [59] and a typical rate coefficient for positive–negative ion recombination (k_r) 10^{-9} cm^3/s, the negative ion density decays two orders of magnitude in 1 ms and remains above ~10^{12} cm^{-3} for PRF > 1 kHz. Actually, the recombination time is approximately equal to the time interval of the 100 kHz pulse repetition frequency consistent with the strong variation in the applied voltage to achieve breakdown between 10 and 100 kHz.

The presence of singlet delta oxygen ensures that a minimum electron density is sustained between the voltage pulses. Considering a quasi-steady state of reaction R_1 and R_5, while assuming a minimum constant negative ion density of 10^{12} cm^{-3}, yields a lower limit estimate of the ratio of electron and negative ion density.

$$\frac{[e^-]}{[O_2^-]} = \frac{k_5[O_2(a^1\Delta_g)]}{k_1[O_2][M]}. \tag{8}$$

For a typical $O_2(a^1\Delta_g)$ density of ~10^{14} cm^{-3} in air DBDs [56], the ratio of $[e^-]/[O_2^-]$ is estimated to be ~0.003. This simple estimate confirms that an electron density larger than 10^9 cm^{-3} can be sustained for PRFs (> 1 kHz), explaining breakdown can be achieved for applied voltages below the electric field-induced detachment threshold voltage.

3.1.2 | Impact of Number of Pulses

Figure 4a shows the applied voltage for which breakdown is achieved at atmospheric pressure for various PRFs, for different numbers of applied voltage pulses, N = 1, 10, 50, 100 and continuous wave (CW) mode. The power supply was limited to operate in continuous mode for 100 kHz PRF at atmospheric pressure; therefore, 1000 pulses were considered as CW exclusively for this case. At a 0.1 kHz PRF, the effect of the number of pulses is negligible, showing breakdown voltages identical to single-pulse conditions (~14.5 kV). However, with continuous pulse application, a reduction in breakdown voltage is observed, indicating the impact of species accumulation and memory effects. For PRFs of 1–10 kHz, the breakdown voltage decreases progressively as the number of applied pulses increases. Specifically, with 10–100 pulses, the breakdown voltage reduces to approximately 14 kV, demonstrating an impact of the accumulation of species from previous discharges. At CW, the breakdown voltage further decreases significantly to approximately 9–10 kV, underscoring the long-term multi pulse accumulation of plasma-produced species or gas heating. A significant reduction in breakdown voltage (~8 kV) is observed at PRFs of 50–100 kHz with pulse numbers ranging from 10 to 50. Increasing the number of pulses from 100 to CW mode results in further reduction of the breakdown voltage (~6 kV). These findings emphasise that at PRFs ≥ 10 kHz, accumulating 50–100 voltage pulses is sufficient to significantly lower the breakdown voltage due to the accumulation of plasma produced species over multiple pulses. The effect is significant when the time between two pulses is ≤ 10 μs, which is similar to the lifetime of negative ions and consistent with the previous explanation of the memory effect.

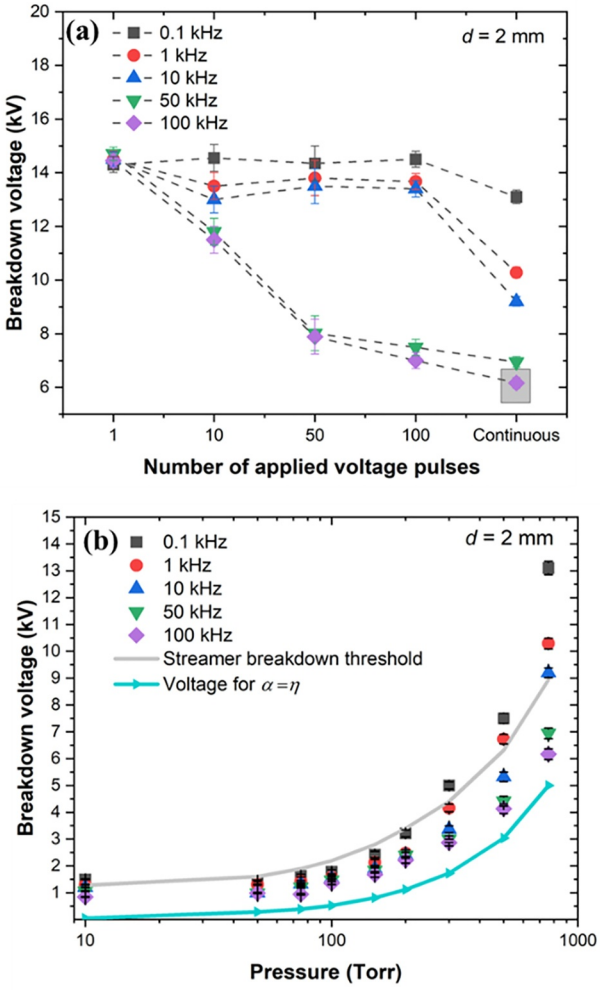

FIGURE 4 | Applied voltage required to achieve breakdown for (a) single pulse to continuous operation for various PRFs at atmospheric pressure and (b) various pressures for different PRFs in continuous operation.

3.1.3 | Impact of Pressure

Figure 4b shows the applied voltage required to achieve breakdown plotted as a function of pressure for various PRF. Continuous pulses were applied to achieve the breakdown, except for the case of 100 kHz at a pressure of 760 Torr where the data is recorded by sending 1000 voltage pulses due to the limitations of power supply at 100 kHz in continuous mode. The trend resembles a DC Paschen breakdown curve for which the breakdown voltage increases with increasing pressure, a typical behaviour observed across all PRFs. However, Paschen breakdown involves secondary electron emission from the cathode and is not applicable on the timescales investigated in this work. Notably, at higher PRFs, volume charge accumulation facilitates easier breakdown at electric field strengths lower than streamer breakdown thresholds. However, this effect is less pronounced at lower pressures (approximately 10–50 Torr), where ion and electron losses due to diffusion become more significant. Considering the N_2^+ diffusion coefficient (D_{ion}) in atmospheric room temperature air is 0.05 cm^2/s [15, 60], the characteristic timescale of ion diffusion inside the discharge gap of $d = 2$ mm is decreasing from ~8 ms at 760 Torr to 0.1 ms at 10 Torr. Electric field-induced detachment time scales inversely with the gas density; therefore, at low pressures, the electron detachment rate slows down by two orders of magnitude as compared to atmospheric pressure and detachment plays a more limited role in breakdown formation at reduced pressures [61]. Although the above discussion focuses on volume memory effects, surface charge accumulation across multiple voltage pulses can also impact the breakdown process.

3.2 | Effect of PRF on Energy Coupling Into the Plasma

Estimation of the energy coupling between the power source and the plasma load is crucial for many applications, especially under the constraints of nanosecond-scale pulse widths and rapid rise times. Effective energy coupling is influenced by factors such as the geometrical arrangement of electrodes, gas composition, and the presence of dielectric materials. To better understand this coupling, the pulse energy was experimentally measured using the combination of D-dot/B-dot sensors and a BCS sensor as described in the methods section. These measurements provide critical insights into the energy dynamics within the plasma, enabling a more precise evaluation of how pulse parameters such as PRF and pulse number within a burst impact energy transfer.

The voltage and current waveforms for an 8 kV pulse are depicted in Figure 5a, whereas the power and cumulative energy waveforms are shown in Figure 5b. The waveforms were recorded at a PRF of 100 kHz for the 100th pulse within a burst consisting of 100 cycles. The main pulse exhibits a rise time of 10 ns and a FWHM of (18 ± 3) ns. The current measured using the B-dot sensor is the total current, comprising both a capacitive (displacement) and a resistive (conduction) component. A sharp change in the current is observed due to the 'reverse discharge' occurring at the falling edge of the pulse, caused by residual space charges and accumulated surface charges generated by the primary discharge. The estimated steady state pulse energy (E_p) is 4 mJ for this case. In Figure 5c, a typical BCS signal for a voltage discharge pulse (for V_{HV} = 8 kV) is presented. The grey shaded areas mark the voltage pulses generated from the pulser named 'FWD' pulse whereas the second peak (1st REF pulse) in the opposite polarity and the other voltage pulses are reflected from the load and travel back towards the pulser. It is noteworthy that a second small voltage peak, observed close to the first peak during the pulse fall time, is attributed to reverse discharge and is also observed in the B-dot signal. For a discharge voltage of 8 kV and a PRF of 100 kHz at the 100th pulse, the estimated forward pulse energy $E_{p,FWD}$ = 13.5 mJ and 1st reflected pulse energy $E_{p,REF}$ = 9 mJ. E_p was calculated by subtracting $E_{p,REF}$ from $E_{p,FWD}$, yielding (4.5 ± 0.3) mJ. Multiple reflections can be considered for a more precise calculation of the deposited energy. Results from both independent power measurement diagnostic methods are comparable and show good agreement within an error margin of 10%. This confirms the accuracy of the calculated pulse energy in this study. The discharge repeatability remained high, with no significant variations observed in day-to-day experiments.

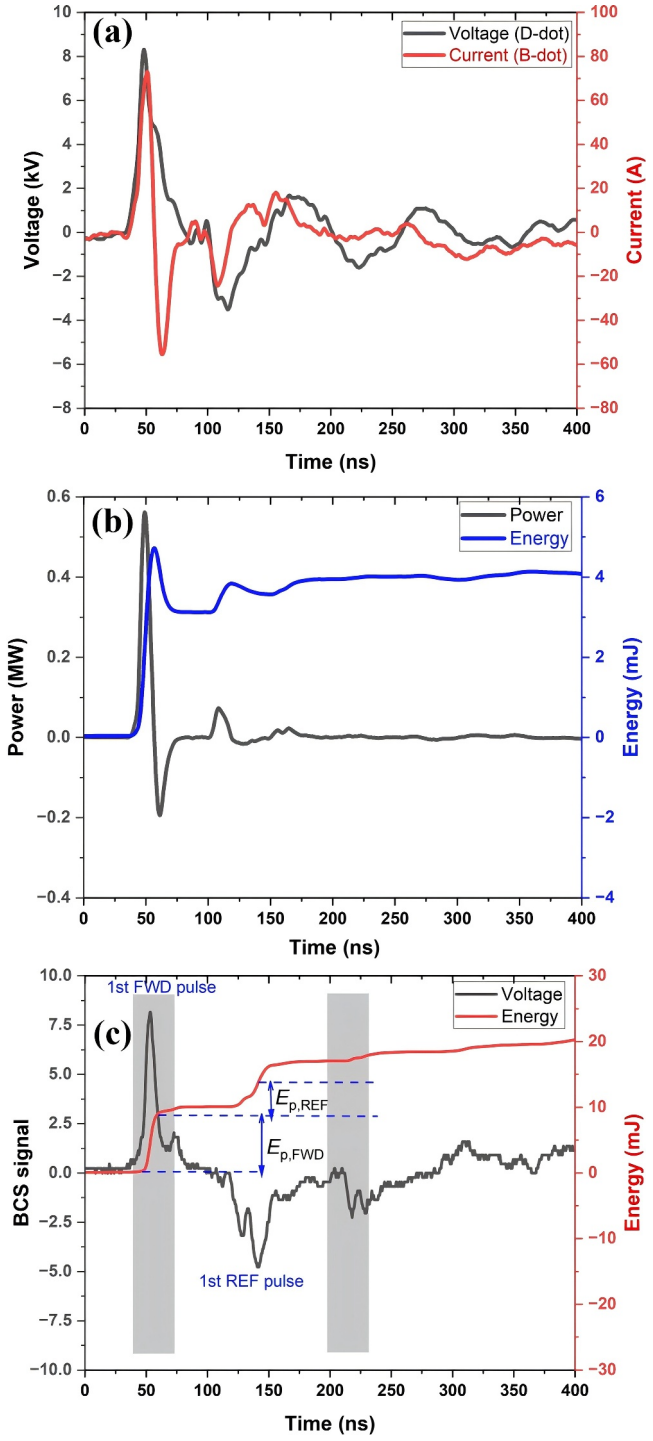

FIGURE 5 | Voltage, current, power and cumulative energy waveforms for an 8 kV pulse. (a) Voltage and current waveforms recorded by the D-dot and B-dot, respectively. (b) Power and cumulative energy waveforms from the discharge at atmospheric pressure measured using D-dot and B-dot sensors. (c) Voltage derived from the BCS and corresponding energy measurement.

Further, by analysing the BCS voltage signals for different pulse numbers and PRFs, we discerned trends in how the plasma load interacts with the power source and affects the energy coupled into the discharge. Specifically, high reflected pulse voltage indicates low energy transfer to the plasma, leading to inefficiencies in energy utilisation. Quantification of the energy dissipated in the plasma load is crucial to understand the behaviour of the discharge. This involves subtracting the energy reflected from the DBD load from the total energy supplied by the pulse source.

Figure 6a shows the BCS voltage signals for varying pulse numbers ($N = 1$, 5, 10, 30, 50, and 100) at a fixed applied voltage of 8 kV and a PRF of 100 kHz. The figure shows that a portion of the applied pulse voltage is reflected from the DBD load, and the amplitude of the reflected pulse into the HV cable differs even when the forward pulse remains consistent with increasing pulse number. Initially, for $N = 1$, the reflection is nearly equal in amplitude to the forward pulse. However, the reflection decreases noticeably already by the 5th pulse.

Similarly, experiments were conducted to examine the influence of PRF on reflected pulses, varying from 0.1 to 100 kHz. Figure 6b demonstrates that at lower PRFs, higher reflections travel back towards the pulser, indicating less efficient energy transfer in the DBD system. This is attributed to weaker pulse-to-pulse coupling at low PRFs, resulting in a predominantly nondissipative capacitive load impedance and consequently larger amplitude pulse reflections. Conversely, at PRFs above 1 kHz, the plasma becomes more resistive and power deposition becomes more efficient, leading to reduced reflected pulse amplitudes due to stronger pulse-to-pulse coupling established by previous discharges. Designing an impedance-matched system is the best way to optimise energy utilisation but is beyond the scope of this work.

To quantify these observations, the pulse energy was determined using electrical methods described above. Figure 6c presents the estimated pulse energy for increasing pulse numbers at various PRFs, with a high voltage variation from 13 to 8 kV to sustain plasma. Two main trends are evident from the plot: firstly, the pulse energy increases within the first few pulses to reach quasi-steady state, after which further increases in pulse number have minimal influence on pulse energy, consistent across all PRFs. Secondly, energy coupling improves with increasing PRF for a given pulse number. This trend reaches a plateau after PRF $\geq$ 50 kHz, with energy coupling enhanced by more than a factor of 2 from 1 to 50 kHz.

3.3 | Discharge Morphology

This subsection discusses the impact of pulse numbers and PRFs on energy deposition into the discharge and how it affects discharge morphology. The analysis is based on images that capture the full 25 mm diameter of the discharge gap. The images provide overall information of the discharge structure but are not intended to study filament morphology.

3.3.1 | Atmospheric Pressure Discharges

Figure 7a shows the discharge at atmospheric pressure for a range of PRFs and pulse numbers allowing us to assess memory effects. For PRFs between 0.1 and 1 kHz, a diffuse discharge is generated with partial filament formation. There is no

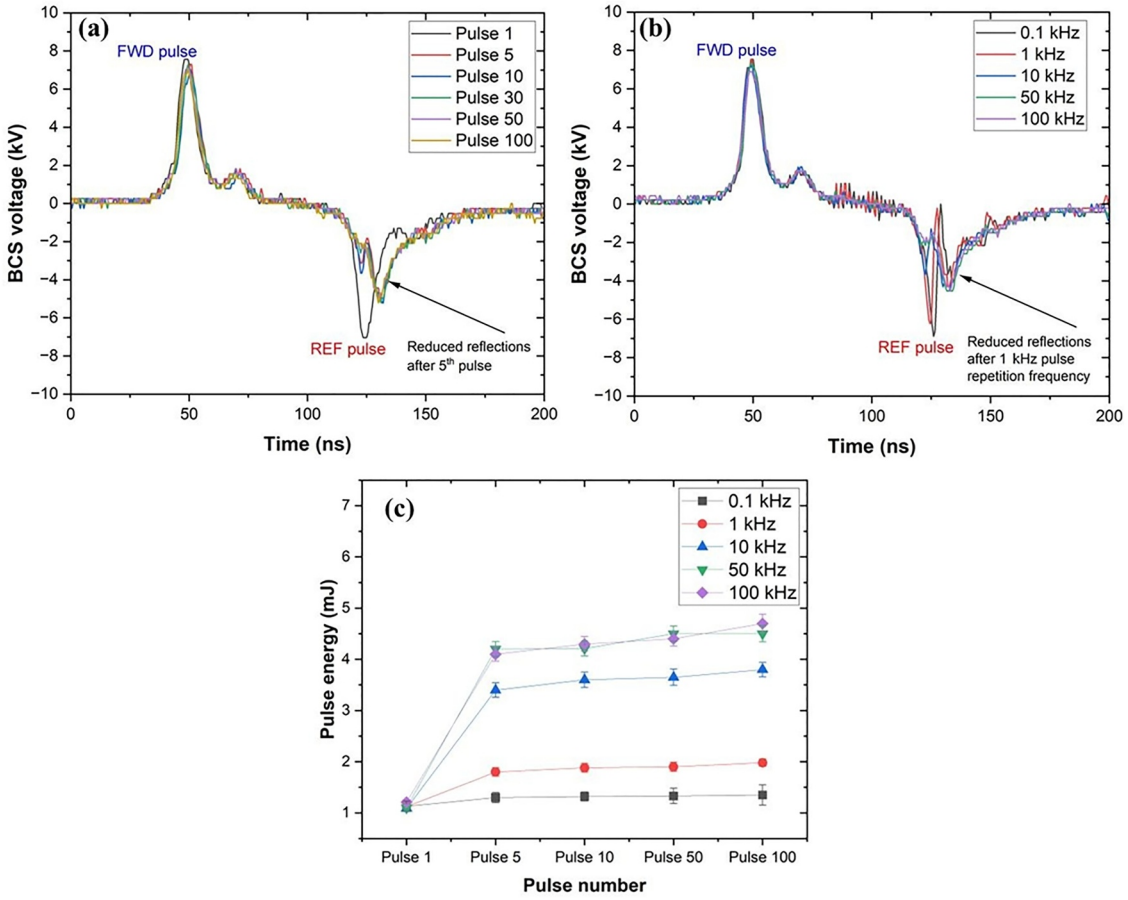

FIGURE 6 | BCS profile shows improved impedance matching for atmospheric pressure air discharge within a single burst of a total of 100 voltage pulses. (a) Pulse number increment at a PRF of 100 kHz. (b) Pulse repetition frequency increment for $N = 100$. (c) Pulse energy estimation for various pulse numbers and PRFs. Mean values are reported and the error bars represent the standard deviation of repeated measurements.

significant variation observed in discharge morphology with changes in pulse numbers under these conditions. Discharge uniformity at low PRFs was obtained even though the discharge fulfils the criterion of streamer formation. This behaviour has been reported by Liu et al., where they showed that discharge uniformity was achieved in the case of significant over-voltages in the discharge gap (conditions for which the applied voltage becomes significantly larger than the streamer breakdown voltage threshold) [22]. The criteria for uniform discharge development were further extended by the requirement that the voltage pulse rise time, τ_{rise}, should be significantly smaller than $dv_d{}^{-1}$ for which the drift velocity is evaluated at the critical electric field. It was found that at a lower electric field value (~400 Td), the discharge develops as a conventional cathode-directed streamer where a non-uniform discharge generated, whereas at higher values of overvoltage an almost uniform discharge was observed [22]. In our case for PRF $\leq$ 1 kHz, the applied voltages were much greater than the critical voltages, thereby following the previously proposed criteria for discharge uniformity. However, with an increase in PRF ($\geq$ 10 kHz), filaments begin to form and lead to nonuniform discharge generation particularly after 10 pulses. The filaments grow stronger and brighter at PRFs of 50–100 kHz, with intense surface discharges (T-shaped filaments) observed after 100 pulses at a PRF of 100 kHz. The results are consistent with the need for an

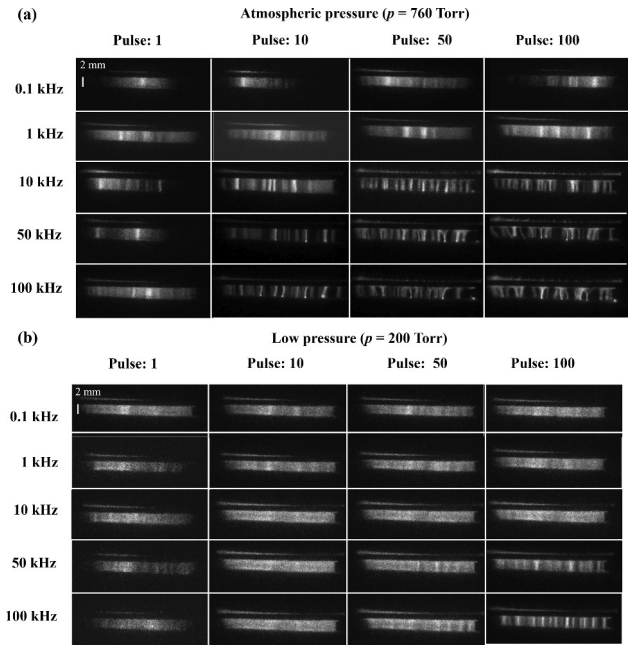

FIGURE 7 | Discharge images at various PRFs. (a) Atmospheric pressure discharge morphology, at V_{HV} ~ (13–8) kV and (b) discharge morphology, at 200 Torr and V_{HV} ~ (3.2–2.8) kV.

overvoltage to generate diffuse nanosecond pulsed discharges but also correlate with memory effects.

3.3.2 | Low Pressure Discharges

Filament formation at atmospheric pressure is a common phenomenon, becoming less pronounced at reduced pressures. Similar experiments at atmospheric pressure were also conducted at low pressure (200 Torr). The discharge images are shown in Figure 7b. At 200 Torr, for PRFs between 0.1 and 100 kHz, the discharge exhibited a diffuse glow-like morphology consistent with high over-voltages. A transition to partial filament formation was observed for $N = 100$ and PRFs of 50 and 100 kHz suggesting the importance of pulse-to-pulse cumulative memory effects.

The trend for pulse energy and discharge morphology is plotted for various PRFs for pressures from 100 to 760 Torr as shown in Figure 8. Operating voltages were chosen that allowed the discharge to be maintained for all PRFs at a fixed pressure.

The atmospheric pressure DBD system could generate ~4.5 mJ pulse energy for 100 kHz PRF. As the voltage requirement for discharge sustainment decreased with pressure reduction, the generated pulse energy also decreased. The discharge is found to be purely diffuse when the operating pressure is lower than 100 Torr for the entire PRF range and becomes partially filamentary for PRF within 50–100 kHz when the pressure increases to 200 Torr as shown in Figure 7b. Furthermore, at higher pressure, the discharge produces more filaments and becomes filamentary at 760 Torr. Only the PRF of 0.1 kHz remained partially diffused at atmospheric pressure. This figure suggests that there might be an energy threshold for diffuse discharge generation around ~0.5 mJ.

In summary, we have observed that the discharge morphology transitions from diffuse to filamentary with an increase in pulse number and/or pulse PRF at constant voltage and pressure. This transition might coincide with the elevated pulse energy at higher PRF, prompting the question of whether the filament formation is primarily due to the higher pulse energy or a reduction in the breakdown voltage.

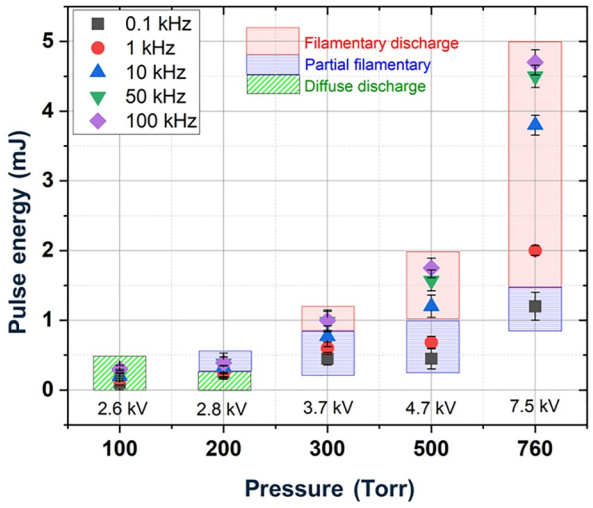

FIGURE 8 | Pulse energy and plasma morphology at various operating pressures. Discharge voltage is mentioned for the corresponding pressure for a PRF of 100 kHz. Data is for $N = 100$.

3.4 | Diffuse to Filamentary Transformation: Influence of Elevated Energy or Memory Effect?

To investigate the role of the memory effect, we analysed the roles of three parameters: gas temperature, pulse energy coupled to plasma and the number of filaments for varying conditions for two different pressures (200 and 760 Torr).

3.4.1 | Low Pressure ($p = 200$ Torr) Case

The gas temperature during the voltage pulse was determined by using the method discussed in Section 2.3. The number of filaments in the parallel plate DBD volume was determined from 2-D images from the discharge's side view. The results provide a valuable comparative analysis that should not be considered as a comprehensive count of all filaments within the discharge volume as only a projection of the filaments on one plane is considered.

To investigate the mechanism causing the memory effect, the pulse energy was kept constant (by adjusting voltage) while varying the PRF for the 100th pulse at 200 Torr. Figure 9a presents the data for a fixed pulse energy, $E_p \approx 0.3$ mJ, showing that the gas temperature remained nearly constant at ~380 K for all investigated PRF values. The notable variation observed in this plot is the onset of filament formation, beginning at 10 kHz

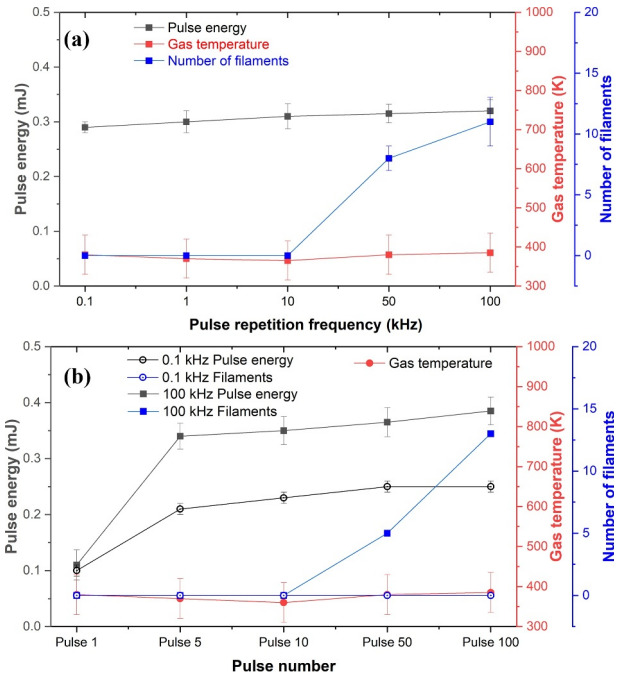

FIGURE 9 | Variation of gas temperature, pulse energy and estimated number of filaments as a function of (a) PRF at a fixed pulse energy (0.3 mJ) for $N = 100$ and (b) pulse number for PRFs of 0.1 and 100 kHz at $V_{HV} = 2.8$ kV. The pressure was 200 Torr.

PRF and significantly increasing up to 100 kHz. This indicates an effect of charge accumulation or species persistence from previous discharges, despite negligible residual heat effects or drop in the breakdown voltage.

Further exploration of the effect of pulse number was conducted at extreme PRF values of 0.1 and 100 kHz (see Figure 9b). In both cases, the gas temperature remained consistent (~380 K), with an observable increase in pulse-to-pulse energy by the 5th pulse. However, significant filament formation was only observed at 100 kHz PRF, starting after the 10th pulse and increasingly thereafter. Moreover, despite a significant increase in pulse energy from the 1st to the 5th pulse, the discharge remained diffuse, indicating that pulse energy alone has no discernible impact on discharge morphology. The transition from diffuse to filamentary discharge appears to be influenced more strongly by the accumulation of plasma produced species over successive pulses.

3.4.2 | Atmospheric Pressure (p = 760 Torr) Case

Similar experiments were conducted at atmospheric pressure, varying the PRF and pulse number. Figure 10a illustrates the scenario for the 100th pulse for different PRFs. Initially, both pulse energy and the number of filaments increase rapidly up to 10 kHz PRF. Beyond this point, the number of filaments stabilises, and the increase in pulse energy slows down (reaching about 4.5 mJ for the 100 kHz case). Simultaneously, the gas temperature shows a linear increase, ranging from 380 to 1000 K for PRF values of 0.1–100 kHz, respectively. This significant temperature variation suggests residual heating from previous discharges. At the ignition of the next pulse, the temperature rise promotes an increase in the reduced electric field, which further enhances ionisation. These conditions seem to facilitate easier filament formation and contribute to an increased filament count.

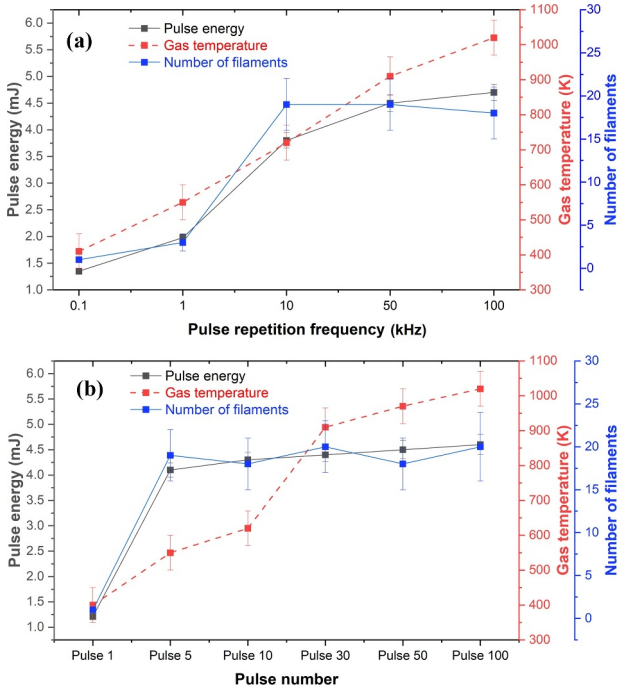

FIGURE 10 | Variation of pulse energy, gas temperature, and estimated number of filaments for atmospheric pressure pulsed discharge at V_{HV} = 8 kV. (a) As a function of pulse repetition frequencies at N = 100 and (b) as a function of pulse numbers at a PRF of 100 kHz.

Figure 10b depicts the variation in pulse energy, gas temperature and number of filaments as a function of pulse number at a PRF of 100 kHz. It shows that pulse energy and the number of filaments stabilise after the 5th pulse. However, there is a noticeable continuous rise in pulse-to-pulse temperature until the 100th pulse. Despite the steady number of filaments after the 5th pulse, their intensity increases progressively with each subsequent pulse, despite constant pulse energy. This trend highlights that gas heating is enabled by the formation of stronger filaments and seems to be a consequence of filament formation, not a cause.

In summary, these experiments reveal that the elevated pulse energy does not significantly influence filament formation or the increase in filament count. Instead, plasma produced species from the previous pulses have the biggest impact on discharge morphology.

4 | Conclusions

We reported breakdown characteristics under varying PRF conditions for a nanosecond pulsed air DBD. Notably, at PRFs ≤ 10 kHz, we suggest that the breakdown occurred primarily through the electron detachment mechanism from negative ions, such as O_2^- ions, supplying secondary electrons critical for streamer formation and satisfying the streamer breakdown criterion. Conversely, at higher PRFs (≥ 10 kHz) the breakdown voltage is well below the conventional streamer breakdown threshold.

Moreover, this study comprehensively explored the interplay between PRF, pulse number, and their impact on both discharge morphology and energy coupling. The experimental results revealed that PRF and pulse number exert significant influence on the discharge morphology, particularly transitioning from diffuse to filamentary patterns with increasing PRF and plasma produced species accumulation. It indicated that high PRFs improve energy transfer into the plasma. Overall, this study advances our understanding of plasma breakdown and dynamics in high pulse repetition frequency nanosecond pulsed DBD systems and paves the path for enhanced control and utilisation of pulsed plasma in diverse applications.

Funding

This work was supported by Advanced Energy Industries Inc. and also partially based upon work supported by the U.S. Department of Energy, Office of Science, Fusion Energy Sciences (Grant DE-SC0020232).

Conflicts of Interest

Denis Shaw is employed by Advanced Energy Industries Inc. who is a sponsor of the research. Mahreen, Dongxuan Xu and Peter Bruggeman have no conflicts to declare.

Data Availability Statement

The data that support the findings of this study are available from the corresponding author upon reasonable request.

References

1. T. Huiskamp, "Nanosecond Pulsed Streamer Discharges Part I: Generation, Source-Plasma Interaction and Energy-Efficiency Optimization," *Plasma Sources Science and Technology* 29, no. 2 (2020): 023002.

2. S. N. Rukin, "Pulsed Power Technology Based on Semiconductor Opening Switches: A Review," *Review of Scientific Instruments* 91, no. 1 (2020): 11501.

3. K. E. Miller, T. Ziemba, J. Prager, J. Picard, and A. Hashim, "Fast Rise Time and High Voltage Nanosecond Pulses at High Pulse Repetition Frequency," in *APS Annual Gaseous Electronics Meeting Abstracts* (2015), GT1.118.

4. B. Huang, C. Zhang, C. Zhang, and T. Shao, "Accumulation Effect of Active Species in Atmospheric-Pressure Plasma Jet Driven by Nanosecond High-Voltage Pulses With MHz Pulse Repetition Rate," *Journal of Physics D Applied Physics* 56, no. 9 (2023): 095201.

5. P. Bruggeman and R. Brandenburg, "Atmospheric Pressure Discharge Filaments and Microplasmas: Physics, Chemistry and Diagnostics," *Journal of Physics D Applied Physics* 46 (2013): 464001.

6. R. Brandenburg, P. J. Bruggeman, and S. M. Starikovskaia, "Fast Pulsed Discharges," *Plasma Sources Science and Technology* 26, no. 2 (2017): 020201.

7. A. Starikovskiy and N. Aleksandrov, "Plasma-Assisted Ignition and Combustion," *Progress in Energy and Combustion Science* 39, no. 1 (2013): 61–110.

8. L. Zhang, K. Wang, K. Wu, et al., "Air Disinfection by Nanosecond Pulsed DBD Plasma," *Journal of Hazardous Materials* 472 (2024): 134487.

9. M. Erofeev, V. Ripenko, M. Shulepov, and V. Tarasenko, "Surface Treatment of Metals in the Plasma of a Nanosecond Diffuse Discharge at Atmospheric Pressure," *European Physical Journal D: Atomic, Molecular and Optical Physics* 71, no. 5 (2017): 1–5.

10. K. Ji, D. Yuan, C. Jin, et al., "Ozone Production in Nanosecond Pulsed Dielectric Barrier Discharge in Synthetic Air: The Effect of Pulse Width," *Vacuum* 230 (2024): 113688.

11. N. Shimomura, M. Wakimoto, Y. Shinke, M. Nagata, T. Namihira, and H. Akiyama, "Generation of Ozone by ns-Width Pulsed Power," in *BEAMS 2002—14th International Conference on High-Power Particle Beams*, Vol. 1 (2002), 345–348.

12. R. Brandenburg, "Dielectric Barrier Discharges: Progress on Plasma Sources and on the Understanding of Regimes and Single Filaments," *Plasma Sources Science and Technology* 26, no. 5 (2017): 053001.

13. T. Matsumoto, D. Wang, T. Namihira, and H. Akiyama, "Energy Efficiency Improvement of Nitric Oxide Treatment Using Nanosecond Pulsed Discharge," *IEEE Transactions on Plasma Science* 38, no. 10 (2010): 2639–2643.

14. R. Patel, J. van Oijen, S. Nijdam, and N. Dam, "Plasma-Assisted Ignition-Stabilized Combustion (PAISC): Benefits, Limitations, and Costs," *Combustion and Flame* 263 (2024): 113401.

15. P. R. Yuri, *Gas Discharge Physics* (Springer-Verlag, 1991).

16. P. J. Bruggeman, F. Iza, and R. Brandenburg, "Foundations of Atmospheric Pressure Non-Equilibrium Plasmas," *Plasma Sources Science and Technology* 26, no. 12 (2017): 123002.

17. A. Fridman, A. Chirokov, and A. Gutsol, "Non-Thermal Atmospheric Pressure Discharges," *Journal of Physics D Applied Physics* 38, no. 2 (2005): R1–R24.

18. S. Nijdam, J. Teunissen, and U. Ebert, "The Physics of Streamer Discharge Phenomena," *Plasma Sources Science and Technology* 29, no. 10 (2020): 103001.

19. S. A. Starostin, P. A. Premkumar, M. Creatore, et al., "On the Formation Mechanisms of the Diffuse Atmospheric Pressure Dielectric Barrier Discharge in CVD Processes of Thin Silica-Like Films," *Plasma Sources Science and Technology* 18, no. 4 (2009): 045021.

20. C. Montijn and U. Ebert, "Diffusion Correction to the Raether–Meek Criterion for the Avalanche-to-Streamer Transition," *Journal of Physics D Applied Physics* 39, no. 14 (2006): 2979–2992.

21. T. Ito, T. Kanazawa, and S. Hamaguchi, "Rapid Breakdown Mechanisms of Open Air Nanosecond Dielectric Barrier Discharges," *Physical Review Letters* 107, no. 6 (2011): 065002.

22. C. Liu, D. Dobrynin, and A. Fridman, "Uniform and Non-Uniform Modes of Nanosecond-Pulsed Dielectric Barrier Discharge in Atmospheric Air: Fast Imaging and Spectroscopic Measurements of Electric Fields," *Journal of Physics D Applied Physics* 47, no. 25 (2014): 252003.

23. S. Liu and M. Neiger, "Excitation of Dielectric Barrier Discharges by Unipolar Submicrosecondsquare Pulses," *Journal of Physics D Applied Physics* 34, no. 11 (2001): 1632–1638.

24. R. Brandenburg, Z. Navrátil, J. Jánský, P. St'Ahel, D. Trunec, and H. E. Wagner, "The Transition Between Different Modes of Barrier Discharges at Atmospheric Pressure," *Journal of Physics D Applied Physics* 42, no. 8 (2009): 085208.

25. D. Z. Pai, G. D. Stancu, D. A. Lacoste, and C. O. Laux, "Nanosecond Repetitively Pulsed Discharges in Air at Atmospheric Pressure—The Glow Regime," *Plasma Sources Science and Technology* 18, no. 4 (2009): 045030.

26. D. Z. Pai, D. A. Lacoste, and C. O. Laux, "Nanosecond Repetitively Pulsed Discharges in Air at Atmospheric Pressure—The Spark Regime," *Plasma Sources Science and Technology* 19, no. 6 (2010): 065015.

27. E. M. Bazelyan and Y. P. Raizer, *Spark Discharge* (CRC Press, 1997).

28. T. Gerling, T. Hoder, R. Bussiahn, R. Brandenburg, and K. D. Weltmann, "On the Spatio-Temporal Dynamics of a Self-Pulsed Nanosecond Transient Spark Discharge: A Spectroscopic and Electrical Analysis," *Plasma Sources Science and Technology* 22, no. 6 (2013): 065012.

29. E. I. Mintoussov, S. V. Pancheshnyi, and A. Y. Starikovskii, "Propane-Air Flame Control by Non-Equilibrium Low-Temperature Pulsed Nanosecond Barrier Discharge," in *AIAA Paper* (2004), 12385–12395.

30. T. Shao, K. Long, C. Zhang, P. Yan, S. Zhang, and R. Pan, "Experimental Study on Repetitive Unipolar Nanosecond-Pulse Dielectric Barrier Discharge in Air at Atmospheric Pressure," *Journal of Physics D Applied Physics* 41, no. 21 (2008): 215203.

31. Y. Zhang and C. Guerra-Garcia, "Discharge Regimes and Transitions in Pulsed Nanosecond Dielectric Barrier Discharges at Atmospheric Pressure," in *AIAA Aviation and Aeronautics Forum and Exposition, AIAA AVIATION Forum 2021* (2021), 3118.

32. S.-H. Kim, U.-H. Yun, and J.-G. Kim, "Characteristics of High-Repetition-Rate Bipolar Pulse DBD Under Various Electrical Conditions in Atmospheric-Pressure Air," *Journal of Physics D Applied Physics* 57, no. 12 (2023): 125206.

33. B. M. Goldberg, I. Shkurenkov, S. O'Byrne, I. V. Adamovich, and W. R. Lempert, "Electric Field Measurements in a Dielectric Barrier Nanosecond Pulse Discharge With Sub-Nanosecond Time Resolution," *Plasma Sources Science and Technology* 24, no. 3 (2015): 035010.

34. S. V. Pancheshnyi, D. A. Lacoste, A. Bourdon, and C. O. Laux, "Ignition of Propane-Air Mixtures by a Repetitively Pulsed Nanosecond Discharge," *IEEE Transactions on Plasma Science* 34, no. 6 (2006): 2478–2487.

35. H. Höft, M. Kettlitz, M. M. Becker, et al., "Breakdown Characteristics in Pulsed-Driven Dielectric Barrier Discharges: Influence of the Pre-Breakdown Phase Due to Volume Memory Effects," *Journal of Physics D Applied Physics* 47, no. 46 (2014): 465206.

36. T. Shao, G. Sun, P. Yan, et al., "An Experimental Investigation of Repetitive Nanosecond-Pulse Breakdown in Air," *Journal of Physics D Applied Physics* 39, no. 10 (2006): 2192–2197.

37. Z. Zhao and J. T. Li, "Integrated Effect on Evolution of Streamer Dynamics Under Long-Term Repetitive Sub-Microsecond Pulses in High-Pressure Nitrogen," *Plasma Sources Science and Technology* 28, no. 11 (2019): 115019.

38. R. Patel, J. van Oijen, N. Dam, and S. Nijdam, "Low-Temperature Filamentary Plasma for Ignition-Stabilized Combustion," *Combustion and Flame* 247 (2023): 112501.

39. R. Patel, J. van Oijen, S. Nijdam, and N. Dam, "On Pulse-to-Pulse Coupling in Low-Temperature Filamentary Plasma-Assisted Ignition in Methane-Air Flows," *Plasma Sources Science and Technology* 32, no. 6 (2023): 065003.

40. Z. Zhao and J. Li, "Repetitively Pulsed Gas Discharges: Memory Effect and Discharge Mode Transition," *High Voltage* 5 (2020): 569–582.

41. S. Nijdam, E. Takahashi, A. H. Markosyan, and U. Ebert, "Investigation of Positive Streamers by Double-pulse Experiments, Effects of Repetition Rate and Gas Mixture," *Plasma Sources Science and Technology* 23, no. 2 (2014): 025008.

42. Y. Li, H. Li, Z. Liu, et al., "Breakdown, Discharge Modes, and Gaseous Recovery of Atmospheric Air With Repetitive 10 Ns Pulses," *Physics of Plasmas* 28, no. 7 (2021): 073510.

43. Y. Luo, *Experimental and Numerical Study of Nanosecond Pulsed Water-Containing Discharges* (University of Minnesota, 2019).

44. M. Simeni Simeni, Y. Luo, and P. J. Bruggeman, "On the Origins of the Continuum Radiation of an Underwater Nanosecond Pulsed Discharge: An Absolute-Intensity Optical Emission Spectroscopy Study," *Plasma Sources Science and Technology* 34, no. 2 (2025): 025003.

45. A. Khomenko, V. Podolsky, and X. X. Wang, "Different Approaches of Measuring High-Voltage Nanosecond Pulses and Power Delivery in Plasma Systems," *Electrical Engineering* 103, no. 1 (2021): 57–66.

46. G. Correale, R. Winkel, and M. Kotsonis, "Energy Deposition Characteristics of Nanosecond Dielectric Barrier Discharge Plasma Actuators: Influence of Dielectric Material," *Journal of Applied Physics* 118, no. 8 (2015): 83301.

47. P. J. Bruggeman, N. Sadeghi, D. C. Schram, and V. Linss, "Gas Temperature Determination From Rotational Lines in Non-Equilibrium Plasmas: A Review," *Plasma Sources Science and Technology* 23, no. 2 (2014): 023001.

48. Anon, *SPECAIR, Software Package, Ver. 3.0* (SpectralFit S.A.S, 2012).

49. T. Liu, I. V. Timoshkin, S. J. Macgregor, et al., "Field-Time Breakdown Characteristics of Air, N_2, CO_2, and SF_6," *IEEE Transactions on Plasma Science* 48, no. 10 (2020): 3321–3331.

50. A. Chachereau and S. Pancheshnyi, "Calculation of the Effective Ionization Rate in Air by Considering Electron Detachment From Negative Ions," *IEEE Transactions on Plasma Science* 42, no. 10 (2014): 3328–3338.

51. Z. Zhao, Q. Gao, and X. Zheng, "Role of Electronegative Gas Admixtures in Streamer Start, Propagation and Branching Phenomena," *Plasma Sources Science and Technology* 14, no. 4 (2005): 645–653.

52. A. Sun, J. Teunissen, and U. Ebert, "The Inception of Pulsed Discharges in Air: Simulations in Background Fields Above and Below Breakdown," *Journal of Physics D Applied Physics* 47, no. 44 (2014): 445205.

53. M. Hao, B. Zhang, X. Li, N. L. Aleksandrov, and E. M. Anokhin, "Electron Detachment From O_2 Ions in Oxygen: The Effect of Vibrational Excitation and the Effect of Electric Field," *Journal of Physics B: Atomic, Molecular and Optical Physics* 44, no. 11 (2011): 115202.

54. A. R. Hoskinson, W. T. Rawlins, K. L. Galbally-Kinney, E. Gong, and J. Hopwood, "Production and Loss of $O_2(^1\Delta_g)$ at Atmospheric Pressure Using Microwave-Driven Microplasmas," *Journal of Physics D Applied Physics* 55, no. 12 (2022): 125208.

55. J. Jiang and P. J. Bruggeman, "Ion Fluxes and Memory Effects in an Ar–O_2 Modulated Radiofrequency-Driven Atmospheric Pressure Plasma Jet," *Plasma Sources Science and Technology* 30, no. 10 (2021): 105007.

56. G. Nayak, J. S. Sousa, and P. J. Bruggeman, "Singlet Delta Oxygen Production in a 2D Micro-Discharge Array in Air: Effect of Gas Residence Time and Discharge Power," *Journal of Physics D Applied Physics* 50, no. 10 (2017): 105205.

57. J. Jiang, Y. A. Gonzalvo, and P. J. Bruggeman, "Spatially Resolved Density Measurements of Singlet Delta Oxygen in a Non-Equilibrium Atmospheric Pressure Plasma Jet by Molecular Beam Mass Spectrometry," *Plasma Sources Science and Technology* 29, no. 4 (2020): 045023.

58. F. C. Fehsenfeld, D. L. Albritton, J. A. Burt, and H. I. Schiff, "Associative-Detachment Reactions of O^- and O_2^- by O_2 ($^1\Delta_g$)," *Canadian Journal of Chemistry* 47, no. 10 (1969): 1793–1795.

59. B. Eliasson, M. Hirth, and U. Kogelschatz, "Ozone Synthesis From Oxygen in Dielectric Barrier Discharges," *Journal of Physics D Applied Physics* 20, no. 11 (1987): 1421–1437.

60. M. A. Lieberman and A. J. Lichtenberg, *Principles of Plasma Discharges and Materials Processing* (John Wiley & Sons Inc., 2005).

61. M. Vass, I. Korolov, and D. Loffhagen, "Effective Ionization Rate in Nitrogen–Oxygen Mixtures," *Journal of Physics D Applied Physics* 46, no. 15 (2013): 155201.